NASA TECHNICAL MEMORANDUM

NASA TM X- 62,227

NASA TM X- 62,227

THE INDUCED MAGNETOSPHERE OF THE MOON
I. THEORY

G. Schubert
University of California, Los Angeles, Calif. 90024

C. P. Sonett
Ames Research Center, Moffett Field, Calif. 94035

K. Schwartz
20858 Collins Street
Woodland Hills, Calif. 91364

H. J. Lee
University of California, San Diego
La Jolla, Calif. 92037

January 1973

(NASA-TM-X-62227) THE INDUCED MAGNETOSPHERE OF THE MOON. 1: THEORY (NASA) 59 p HC $5.00 CSCL 03B

N73-17851

Unclas
G3/30 54909

The Induced Magnetosphere of the Moon

I. Theory

G. Schubert

Department of Planetary and Space Science
University of California, Los Angeles
90024

C.P. Sonett

National Aeronautics & Space Administration
Ames Research Center
Moffett Field, California
94035

K. Schwartz

20858 Collins Street
Woodland Hills, California
91364

H.J. Lee

Department of Applied Physics & Information Science
University of California, San Diego
La Jolla, California
92037

I

ABSTRACT

An analytic solution for the magnetic field in the space defined by a spherical Moon and its downstream cylindrical cavity formed by the solar wind is derived for interplanetary magnetic fields both parallel and perpendicular to the cavity axis. By superposition, the solution is obtained for arbitrary orientations of the interplanetary field. The theory is quasistatic and is formulated in terms of a scalar magnetic potential. Thus the Moon model consists of a core of arbitrary size and infinite electrical conductivity surrounded by a nonconducting shell; the cavity volume is also assumed to be nonconducting. The variation of the magnetic field on the lunar surface, both on the sunlit and on the dark side hemispheres, and on the cavity boundary is presented for various values of core radius. The solution also yields the distribution of currents on the lunar sunlit surface and the surface of the cavity. Theoretical transfer functions are also presented and their variations with position on the lunar surface and with core size are discussed. The results are compared with those of spherically symmetric approximations to lunar magnetic induction.

II

INTRODUCTION

Quantitative measurements of lunar electromagnetic induction by the Apollo 12 surface magnetometer have provided a considerable stimulus towards understanding the role played by the asymmetric plasma environment of the Moon in this phenomenon. Magnetic field fluctuation data, obtained when the surface magnetometer is on the front side, i.e. the side directly exposed to the solar wind or magnetosheath plasma, have been interpreted in terms of a spherically symmetric theory which assumes no scattered electromagnetic radiation [Sonett et al., 1971a, b; Sonett et al., 1972a]. The analytic formulation of this theory was carried out by Schubert and Schwartz [1969, 1972], Schwartz and Schubert [1969] and Blank and Sill [1969]. The no scattering assumption is equivalent to assuming that magnetic fields associated with induced currents in the Moon are confined to the lunar volume. On the front side this condition is approximately correct since waves cannot travel upstream in the supermagnetosonic plasma. Further, magnetometer experiments on the lunar sunlit surface have shown that the fields induced in the lunar interior by the action of fluctuations in the interplanetary magnetic field are strongly confined by the momentum flux of the solar wind [Sonett et al., 1971c]. However, because of the interruption of the solar wind flow by the Moon and the consequent

lack of plasma dynamic pressure on the dark lunar hemisphere, it is likely that magnetic fields induced in the lunar interior leak into the cavity.

Magnetic field fluctuation data, obtained when the surface magnetometer is on the far side within the diamagnetic cavity, have been interpreted in terms of a spherically symmetric theory which assumes vacuum scattering [Dyal and Parkin, 1971; Dyal et al., 1972]. The theoretical formulation of the spherically symmetric vacuum scattering problem is a classic exercise in electrodynamics (see e.g. Stratton, 1941). However, the induced magnetic fields are in fact essentially confined to the body of the Moon and the space of the cavity. Approximate confinement to the interior of the cavity occurs since downstream travelling scattered waves in the supermagnetosonic solar wind are limited to the interior of the Mach cone extending downstream from the limb. A self-consistent confinement current layer therefore exists along the cavity walls and distorts that part of the lunar induced field found on the dark hemisphere. The confinement current system is conceptually distinct from the currents associated with the cavity diamagnetism [Colburn et al., 1967]. Both the confinement currents and the diamagnetic currents are the result of discontinuities in the tangential magnetic field. The model discussed in this paper is restricted to confinement currents.

Lunar magnetic induction at hydromagnetic frequencies is a

global phenomenon; it follows that a theory for the induction should account for asymmetric plasma conditions surrounding the Moon. In this paper, Part I, we present an asymmetric induction theory and compare the results with those of the two spherically symmetric approximations. In Part II, lunar surface magnetometer data will be discussed and interpreted using the asymmetric theory. We note in this connection that Reisz et al. [1972] have considered the asymmetric induction problem for a cylindrical Moon. Their solution was obtained using a numerical finite difference scheme but the lack of detail in their paper makes an evaluation difficult [Sonett et al., 1972b]. The analytic solution of this paper carried out for a spherical Moon shows that the front side spherically symmetric solution is more accurate than the results of Reisz et al. [1972] would indicate.

The solar wind distorts the dipole and higher order multipole parts of the time dependent induced lunar field in a manner somewhat similar to the distortion of the Earth's dipole field by the solar wind. Thus we speak of a time dependent lunar magnetosphere; its boundaries are delineated by the front side lunar surface, the diamagnetic cavity walls and the interior lunar bulk electrical conductivity profile [Sonett and Colburn, 1968; Johnson and Midgley, 1968]. The sunward surface of the Moon corresponds to the Earth's magnetopause. In the case of the Earth's field, the magnetopause is formed where the magnetic pressure of the dipole field is comparable to the dynamic pressure

of the incoming plasma. In the lunar case, the magnetic pressure of the induced fields is insufficient to balance the solar wind dynamic pressure. Rather, the lunar surface, which is a fixed boundary and absorbs much of the incident plasma, marks the sunward extent of the induced field. The lunar magnetosphere concept is supported by the theoretical results presented here and the empirical data of Part II. For example, in this paper we show that for a lunar magnetic field induced by an interplanetary field transverse to the direction of solar wind flow, there are two points on the surface of the sunlit hemisphere where the magnetic field tangential to the surface vanishes. These points are qualitatively similar to the neutral points found on the Earth's sunward magnetopause [Spreiter and Alksne, 1970]; however, for the Moon the positions of vanishing tangential field are not neutral points because the radial field does not vanish there.

The next section gives a description of the theoretical model. Following that we proceed to a discussion of the results of the analysis. Mathematical details are given in the appendices. This will permit the reader mainly interested in the configuration of the distorted induced lunar magnetic field, i.e. the lunar magnetosphere, to avoid the mathematical complexity of the theory.

THEORETICAL MODEL

Induced lunar magnetic field lines must accommodate themselves to an available volume delineated by the front side lunar surface, the cavity boundary and the lunar electrical skin depth profile. A precise radial location of the internal boundary to this volume cannot be determined in general since attenuation of electromagnetic waves occurs over a range of depths. However, an equivalent depth can be defined for a given frequency, such that a correct measure of the inductive response is obtained by considering the Moon to be nondissipative above this depth and perfectly conducting below. Thus the exclusion of fluctuating fields from the lunar interior as a result of cumulative attenuation is modelled with a perfectly excluding core of an equivalent size. The model adopted here is thus a quasistatic one in which the induced lunar field lines are distorted to occupy the space between an infinitely conducting core of radius b and the confining boundaries of the front side lunar surface of radius a and the walls of the cylindrical cavity of radius a which extends downstream from the Moon (positive z-direction). Both the lunar shell of thickness (a-b) and the downstream cavity are nonconducting.

The center of the Moon coincides with the origin of the coordinate system and the axis of the cylinder is the z-axis. We use both spherical coordinates (r, θ, φ) and cylindrical

coordinates (ρ, φ, z). The geometry is illustrated in Figure 1. The space outside the Moon and the cavity is occupied by solar wind or magnetosheath plasma, and magnetic fields, associated with induced currents in the Moon, on the lunar front side surface, or on the cavity boundary, cannot penetrate this region.

At the frequencies of interest, the lunar cavity radius is much smaller than the vacuum wavelengths of electromagnetic waves, thus displacement currents are negligible. In the non-conducting shell of the Moon, and in the cavity, the magnetic field is derivable from a scalar potential Ω

$$\underline{H} = \nabla\Omega \quad , \qquad (1)$$

$$\nabla^2\Omega = 0 \quad . \qquad (2)$$

The theory assumes that the external fluctuating field is spatially uniform. Most of the frequencies of interest are sufficiently low so that the solar wind sweeps through an appreciable distance in times comparable to the periods associated with the induction. For example at a frequency of 10^{-2} Hz, a relatively high frequency for lunar surface magnetometer observations, and a solar wind speed of 400 km/sec, the solar wind travels 4×10^4 km or about 20 lunar radii in a wave period. Because of the cavity deformation of the induced

field, dipole and higher order multipoles of the induced field are present; however, the high frequency modification of these multipoles, due to spatial nonuniformity in the external field which is present at sufficiently short time scales, is not included in the theory.

Everywhere external to the Moon and cavity we assume the magnetic field to be uniform, of magnitude unity (without loss of generality), and oriented either normal to the cylindrical axis e.g. in the y-direction, or parallel to the cavity axis, i.e. in the z-direction. By superposition, the solution for an arbitrarily oriented external magnetic field can be obtained from the fundamental solutions presented here. The boundary conditions to be satisfied by the solutions of (2) are continuity of the normal component of magnetic field on the cylindrical boundary and the front side lunar surface and zero magnetic field normal to the surface of the inner core. In addition, the magnetic field in the cavity and in the insulating shell must be continuous on the far side lunar surface.

The possible effects of diamagnetism on the induced field are not included. Diamagnetism influences the steady field by leading to an increase of the steady interplanetary field inside the cavity. We are concerned here only with the time varying field, but it also might be influenced by fluctuations of the intensity of diamagnetism as the solar wind parameters vary. We also neglect the effects, other than confinement,

of the undoubtedly complex processes occuring in the interaction layer of the cavity walls.

DISCUSSION OF RESULTS

The details of the analytic solution are presented in the appendices. Appendix A deals with the case of the external magnetic field perpendicular to the cavity axis and appendix B considers the external field aligned along the cavity axis. For each orientation of the external field we write the scalar magnetic potential and the fields in the nonconducting lunar shell in terms of expansions in spherical harmonics. Similarly, in the cavity, the potentials and fields are given by expansions in terms of cylindrical eigenfunctions of the Laplace equation. This facilitates the application of the boundary conditions on the cavity walls. The solutions in the cavity are then written in terms of spherical harmonics with the aid of an identity which permits expansion of cylindrical eigenfunctions in terms of spherical ones. Finally, application of the appropriate boundary conditions on the lunar surface r=a determines the solutions.

In addition to the asymmetric solutions, formulas for the magnetic fields in the spherically symmetric vacuum SSV approximation (A.10) - (A.13) and (A.48) - (A.50) and the spherically symmetric plasma SSP approximation (A.6) - (A.9) and (A.45) - (A.47) are given in the appendices. In the SSV case, the field is just the superposition of the uniform external field and an induced dipole which prevents the external field from penetrating

the infinitely conducting core. In the SSP case, the solution is similar except for an amplification of the strength of the induced dipole as a result of compression of the induced field into the lunar shell.

If the radius of the lunar core is zero the magnetic field is everywhere the uniform field existing outside the space of the Moon and cavity. This may be seen in the case of the external field normal to the cavity axis, for example, from (A.28) and (A.29). With b=0, $\alpha_1=1$ and the equations for the coefficients C_ℓ are homogeneous. Thus $C_\ell \equiv 0$ and from (A.15) - (A.17) it follows that the magnetic field in the cavity is simply the uniform external field. Further, from (A.30) and (A.31) it is clear that $A_1=1$ and $A_\ell=0$ for $\ell \geq 2$. Using (A.5) we find $B_\ell=0$ for all ℓ . Thus the field inside the Moon is indeed the uniform field of the external space.

In the following we present results showing magnetic fields and transfer functions for different external field orientations and core radii between 0.5 and 0.9 lunar radii. Differences between the spherically symmetric approximations and the exact solutions of this paper generally become increasingly significant as the core radius increases, corresponding to waves whose attenuation is progressively more significant at shallower depths in the Moon. Thus the inadequacy of spherically symmetric approximations will be most serious at the high frequency end of the spectrum accessible with the lunar surface magnetometers.

Lunar Surface Fields for External Field Parallel to Cavity Axis

Figure 2 shows the radial component of the total magnetic field on the dark side lunar surface ($r=a$), $0<\theta<\pi/2$, as a function of θ. Also shown is the radial magnetic field computed from the SSV approximation. All fields are scaled to an external field of unit amplitude. On the sunward side of the Moon the radial magnetic field is identical to the radial component of the external field, $\cos\theta$. In the SSV approximation the radial field increases monotonically from zero at the limb to a maximum at the antisolar point and shows a $\cos\theta$ dependence. Also, as the core radius increases, for a given θ, the radial SSV field decreases. For all b/a the radial field is larger than that of the SSV approximation, the difference becoming more significant as b/a increases. For b/a = 0.5, 0.6, and 0.7 the radial field increases monotonically from zero at the limb to a maximum at the antisolar point. However, for b/a = 0.8 and 0.9 the radial field increases to a maximum very near to the limb and subsequently goes through a minimum as θ approaches 0°. As a result, near the limb the field decreases with increasing core size, whereas near the antisolar point the field increases with increasing core size. The increase in the radial field above the SSV value, the local minimum in the field seen near the antisolar point and the field maximum near the limb for large cores can all be understood in terms of the distortion of the induced field which adjusts to the available space defined by the

nonconducting shell and the cavity. For the larger values of b/a the combined fields of the cavity and interior currents add to raise the total to a very large value near the terminator. Away from the terminator, i.e. towards the antisolar point, the total field drops quickly but never to a value equal to the SSV case. Thus either the cavity edge field is of very high order and therefore of short range, or its direction is rapidly changing so that its contribution to the radial component of the lunar far side surface field attenuates rapidy as $\theta \rightarrow 0$, or both these effects are present.

Figure 3 shows the θ-component of the total field at the surface of the Moon normalized as before to unity driving field and the θ-component of the SSV field for varying b/a. The SSP fields on the front side lunar surface are virtually identical to the fields of the exact solution. Front side amplification of this field is thus negligibly affected by the day-night asymmetry of the lunar plasma environment. On the lunar far side, H_θ is also amplified considerably above its SSV value, amplification increasing with increasing b/a and proximity to the limb. As one might expect the effect of cavity confinement of the far side field dominates near the terminator where H_θ attains a maximum.

It is interesting to note that the calculations show the maximum to move slightly forward of the terminator with increasing b/a. For b/a = 0.9 this maximum is about 3-4 degrees ahead

of the limb (a precise location of the maximum would require evaluating the field on a finer θ scale than was done for this paper). This is a consequence of field line redistribution internally in the Moon as a result of the day-night asymmetry of the space external to the Moon. Figure 3 clearly shows a day-night asymmetry in H_θ which becomes more pronounced for increasing b/a. This is readily understandable since the compressive effects of the solar wind are different from those of confinement by the cavity. Lastly we note that for the case of the external field aligned along the cavity axis H_φ vanishes and H_r and H_θ are independent of φ because of azimuthal symmetry. It is remarkable that for the external field aligned case the front side lunar surface magnetic field is practically identical to the SSP approximation while the dark side surface field is significantly different from the SSV field even for large b/a !

Lunar Surface Fields for External Field Perpendicular to Cavity Axis

We next turn to the configuration where the external magnetic field lies normal to the cavity axis. Figure 4 shows the radial component of the field on r=a vs. θ between the antisolar point and the terminator together with the SSV approximation to this field. At the limb H_r must be unity to preserve continuity of the normal component of the magnetic field. Similarly on the sunward side of the Moon this continuity condition prescribes the variation of H_r with θ to be that of the external field. We

note that $H_r \propto \sin\varphi$ so that the variation of H_r shown is for the y-z plane. Alternatively, for an external field in the x-direction the variation of H_r in Figure 4 would be for the x-z plane.

The dependence of H_r on θ is very different from that of the SSV approximation. Near the antisolar point the asymmetric theory gives values of H_r which are smaller (increased induction) than those found from the SSV theory. However, the situation reverses as the terminator is approached where the values of H_r are larger than the SSV values. The changeover takes place at a value of θ determined by the size of the core; as b/a is increased the crossover occurs nearer the limb. Further the SSV radial functions are concave downwards everywhere on the dark side while the asymmetric calculations show radial functions which display upward concavity over large θ intervals. It is particularly interesting to note the case of b/a = 0.9 where H_r for asymmetric induction is nearly zero over a range of θ up to 60° from the antisolar point. This can be understood by noting that the distortion of field lines around the infinitely conducting core must be accommodated entirely within the cavity space, while in the SSV approximation the field line distortion is more gradual and can occur in the entire space external to the core.

Figure 5 shows the calculations for H_θ which is $\propto \sin\varphi$ (see Appendix A). This figure views H_θ in the plane $\varphi = \pi/2$, i.e. the plane defined by the external field and the cylinder axis.

For convenience we can think of the forcing field to lie in the plane of the ecliptic, which then means that H_θ is measured equatorially about the Moon. It is clear however that the plane as defined above can take on any orientation that includes the cylinder axis. For comparison, Figure 5 also shows the SSV dark side field for b/a = 0.9 and the SSP front side fields for b/a = 0.8 and 0.9. The fields on the front side are generally smaller than the SSP fields. For b/a = 0.9 the differences between actual and SSP fields are largest and amount to nearly 20 per cent at the subsolar point. The differences diminish as b/a becomes smaller. On the dark side H_θ is larger than the SSV approximation. There is considerable cavity amplification of H_θ which can increase as the limb is approached from the antisolar point. The SSV approximation always yields a monotonic decrease of H_θ with proximity to the limb.

An important aspect of the distortion introduced by the asymmetry is that H_θ vanishes for a value of $\theta > 90°$, the zero of H_θ occuring more forward of the limb for increasing b/a. This is qualitatively similar to the case of the Earth's magnetosphere as discussed in the introduction. Generally speaking the dynamic pressure of the solar wind is so much greater than the pressure of the induced field that one should think in terms of field line redistribution here rather than sweeping back of field lines to the dark side by the action of the solar wind, as is often mentioned as the mechanism for the formation of the Earth's

magnetic tail. The case b/a = 0.9 shows a nonmonotonic variation in H_θ on the dark side of the Moon which is attributable to the θ-component of the summed fields of the cavity and core currents peaking at an angle $\theta<90°$. This effect essentially disappears for small b/a. The decrease in the sunward response of the Moon from that of the SSP approximation is attributed to redistribution of field lines from the front to the back.

A discussion of the field H_φ is not presented here since it will be seen that H_φ can be viewed as being identical to the North-South transfer function which is discussed in a later section.

Magnetic Fields on the Cavity Boundary

We have computed the magnetic fields along the walls of the idealized cavity for the two cases of the external field along and normal to the cavity axis. In the next two figures we use cylindrical coordinates to describe the magnetic field. Figure 6 shows the field H_z on the cavity wall for the case of aligned external field as a function of distance along the cavity from the terminator. The abscissa also shows the angle θ corresponding to the varying distance. Since the normal component of magnetic field is required to be continuous on the cavity wall, $H_\rho = 0$. Also because of azimuthal symmetry H_φ vanishes. The field is a maximum at the terminator and decreases with distance along the cavity, becoming vanishingly small for distances in

excess of about one lunar radius downstream from the limb, corresponding to θ of $\approx 45°$. Also H_z increases in magnitude for larger b/a. Azimuthal surface currents of density $K_\varphi = H_z$ (MKS units are understood) flow on the cavity wall and are responsible for the cavity confinement of the induced fields on the dark side. As in the case of the field, the current density attains its maximum value at the terminator. In the neighborhood of the limb the cavity wall currents are of the same order of magnitude as those which flow on the sunward side in response to the confinement there of the induced magnetic field. The surface current density on the sunlit hemisphere can be found from $K_\varphi = -\sin\theta - H_\theta$.

We turn next to the case of the external magnetic field perpendicular to the cavity axis. Figure 7 shows the magnetic fields H_z and H_φ along the cavity walls for this case. The field component H_ρ is simply that component of the external field by continuity of H_ρ at $\rho=a$. Note that $H_\varphi \propto \cos\varphi$ and $H_z \propto \sin\varphi$. Thus we view H_φ in the plane which includes the cavity axis and the normal to the external field, and we view H_z in the plane which includes the cavity axis and the external field. The field H_z peaks at about 0.5 lunar radius downstream from the terminator. The importance of the ratio b/a in determining the magnitude of the cavity wall fields is apparent. In this case two current components coexist on the cavity walls. Azimuthal currents of density $K_\varphi = H_z$ are found as in the aligned

field case and we find this circulating current system peaking downstream at 0.5 lunar radius. Additional currents flow in the z-direction with density $K_z = H_\varphi - \cos\varphi$. The current system on the cavity boundary is of course continuous at the terminator with the current system on the sunward side of the Moon which is given by $K_\varphi = \cos\theta \sin\varphi - H_\theta$ and $K_\theta = - H_\varphi + \cos\varphi$. No dissipation arises from these currents and they are to be regarded as Hall currents flowing across the local field. Currents flowing across the front surface of the Moon to conform with the confinement requirement close in a complex pattern over and under the lunar cavity. Cavity compression of induced fields may be attributed to the currents K_z, K_φ on the cavity boundary.

Transfer Functions

For comparison to experimental data as will be done in Part II it is convenient to describe the lunar response in terms of transfer functions, i.e. ratios of the observed field components to corresponding components of the external field. The empirical data presented in Part II is given in terms of radial or local vertical, North-South and East-West transfer functions. The directions are all local at the site of the Apollo 12 surface magnetometer which is essentially in the ecliptic plane. Contributions to the North-South transfer function can only be made by an external field which is perpendicular to the ecliptic plane. Thus the North-South transfer function is identical to

the field H_φ viewed in the ecliptic plane and driven by an external field of unit amplitude which is normal to the cavity axis and the ecliptic plane. The North-South transfer function is independent of the absolute spatial orientation of the external field as long as it has some nonzero component normal to the ecliptic plane.

Figure 8 shows the North-South transfer function calculated from the asymmetric theory as a function of θ together with the SSV and SSP values for comparison. Both the SSV and SSP approximations to this transfer function are independent of solar longitude (solar longitude or local time at the site of the surface magnetometer is identical to θ in this view of the North-South transfer function). For the SSP approximation we find from (A.8) or (A.9) that the tangential transfer function is

$$1 + \frac{3\, b^3/2}{a^3 - b^3} \quad ,$$

and for the SSV approximation it follows from (A.12) or (A.13) that the tangential transfer function is

$$1 + \frac{b^3}{2a^3} \quad .$$

The effects of asymmetric confinement stand out clearly. As in the discussion of the fields, the larger b/a, the greater the

departure of the asymmetric transfer function from the spherically symmetric approximations. We note that confinement is strongest on the sunward side of the Moon, though not as great as that predicted by the SSP approximation. The reduced amplification on the front side below the SSP value can be understood in terms of the leakage of induced field lines into the cavity space and the redistribution of front side field lines to the back with an accompanying decrease in front side compression. Amplifications are in agreement with the values found experimentally (see Part II). The values of the transfer function decrease monotonically as one moves from the subsolar towards the antisolar point indicating that effective confinement becomes less perfect as the dark side of the Moon is approached. Nevertheless, it can be seen that in spite of the assumption of perfect vacuum in the lunar cavity, there is substantial amplification of the North-South magnetic field on the dark side, where values of amplification are always larger than those of the SSV approximation. This increase in the far side amplification above the SSV value can be understood in terms of cavity compression of the induced field. For $b/a > 0.8$ the amplification is everywhere greater than the theoretical high frequency limit (1.5) for a conducting Moon in vacuum.

Unlike the North-South transfer function, the radial and East-West transfer functions depend on the absolute orientation of the external field. External fields in the ecliptic plane induce magnetic fields which determine these transfer functions.

Since these external fields can be arbitrarily oriented in the ecliptic plane, the radial and East-West transfer functions cannot be a-priori defined. Their values depend on the relative contributions of external field components parallel and perpendicular to the cavity axis.

As an example we show the radial transfer function for an external field which is at 45° to the cavity axis and in the ecliptic plane and $\varphi = 90°$. Figure 9 shows this transfer function for varying b/a as a function of θ. The boundary condition on the normal component of the magnetic field requires that the radial field component be continuous across the front surface of the Moon so that on the entire front side this transfer function is unity for any b/a. On the dark side of the Moon a minimum is seen at about 30 degrees away from the antisolar point. As before the variation in the transfer function increases with b/a. Note that the transfer function in the SSV approximation is independent of solar longitude (as in the case of the North-South transfer function solar longitude or local time is identical to θ) and is given by $1 - \frac{b^3}{a^3}$ (see (A.49)).

At the subsolar and antisolar points, H_θ , H_φ and the tangential (North-South and East-West) transfer functions are identical. Only external fields normal to the cavity axis induce fields which contribute to these quantities. Figure 10 shows the tangential transfer functions at the antisolar and subsolar points together with the appropriate spherically

symmetric approximations vs. b/a. At the subsolar point the transfer function is smaller than the SSP approximation, the difference being negligible for small cores, i.e. low frequency waves, and important for large cores, i.e. high frequency waves which damp at relatively shallow depths. At the antisolar point the transfer function is larger than the SSV approximation, the difference becoming more significant as the core size increases.

The variation with b/a of the radial transfer function at the antisolar point is presented in Figure 11. The SSV approximation to the transfer function is consistently smaller than the radial transfer function of the asymmetric theory. For a given lunar conductivity model the SSV approximation overestimates the induction.

Finally in Figure 12 we show the North-South transfer function at the limb vs. b/a. The radial transfer function at the limb is unity and the East-West transfer function at the limb is dependent on external field orientation. Neither the SSP nor SSV approximations to the North-South transfer function are a-priori expected to be good at the terminator. Both approximations are also shown in the figure. The transfer function has values intermediate between the SSV and SSP approximations. The North-South magnetic field shows considerable amplification at the limb with values closer to those of the SSP than to those of the SSV approximation.

CONCLUSIONS

The analytic solution of this paper predicts the ways in which the confinement attributable to the diamagnetic cavity influences lunar magnetic induction and permits a quantitative assessment of the importance of these effects for various frequencies and for both sunward and dark hemisphere transfer functions. The results will be used in Part II to compare the theory with experimental transfer functions for both sunward side and dark side data.

Field line leakage into the cavity and the internal redistribution of field lines from the front side of the Moon to the night side contribute to a reduction of the sunward side field line compression from that which would be predicted by the spherically symmetric plasma approximation. Cavity compression of field lines, consistent with surface currents on the cavity boundary, acts to amplify the tangential magnetic fields and significantly alters the radial magnetic field on the lunar dark side from the prediction of the spherically symmetric vacuum approximation. These effects are most important for waves whose equivalent exclusion depths are small.

ACKNOWLEDGMENT

This work was supported in part under NAS2-6791. We thank our colleagues D.S. Colburn and B.F. Smith for their interest and helpful comments on this work.

REFERENCES

Abramowitz, M., and I.A. Stegun, editors, Handbook of Mathematical Functions, National Bureau of Standards Applied Mathematics Series 55, p. 411, 1964.

Blank, J., and W.R. Sill, Response of the Moon to the time varying interplanetary magnetic field, J. Geophys. Res., 74, 736-743, 1969.

Colburn, D.S., R.G. Currie, J.D. Mihalov, and C.P. Sonett, Diamagnetic solar wind cavity discovered behind Moon, Science, 158, 1040-1042, 1967.

Cooke, J.C., Some relations between Bessel and Legendre functions, Monatshefte fur Math., 60, 322-328, 1956.

Dyal, P., and C.W. Parkin, Electrical conductivity and temperature of the lunar interior from magnetic transient response measurements, J. Geophys. Res., 76, 5947-5969, 1971.

Dyal, P., C.W. Parkin, and P. Cassen, Surface magnetometer experiments: internal lunar properties and lunar field interactions with the solar plasma, Proc. Third Lunar Sci. Conf., Vol. 3, The M.I.T. Press, in press, 1972.

Johnson, F.S., and J.E. Midgley, Notes on the lunar magnetosphere, J. Geophys. Res., 73, 1523-1532, 1968.

Reisz, A.C., D.L. Paul and T.R. Madden, The effects of boundary condition asymmetries on the interplanetary magnetic field-moon interaction, The Moon, 4, 134-140, 1972.

Schubert, G., and K. Schwartz, A. theory for the interpretation of lunar surface magnetometer data, The Moon, 1, 106-117, 1969.

Schubert, G., and K. Schwartz, High-frequency electromagnetic response of the Moon, J. Geophys. Res., 77, 76-83, 1972.

Schwartz, K., and G. Schubert, Time-dependent lunar electric and magnetic fields induced by a spatially varying interplanetary magnetic field, J. Geophys. Res., 74, 4777-4780, 1969.

Sonett, C.P., and D.S. Colburn, The principle of solar wind induced planetary dynamos, Phys. Earth and Plan. Int., 1, 326-346, 1968.

Sonett, C.P., D.S. Colburn, P. Dyal, C.W. Parkin, B.F. Smith, G. Schubert, and K. Schwartz, Lunar electrical conductivity profile, Nature, 230, 359-362, 1971a.

Sonett, C.P., G. Schubert, B.F. Smith, K. Schwartz, and D.S. Colburn, Lunar electrical conductivity from Apollo 12 magnetometer measurements: compositional and thermal inferences, Proc. Second Lunar Sci. Conf., Geochim. Cosmochim. Acta, Suppl. 2, Vol. 3, 2415-2431, The M.I.T. Press, 1971b.

Sonett, C.P., P. Dyal, C.W. Parkin, D.S. Colburn, J.D. Mihalov, and B.F. Smith, Whole body response of the Moon to electromagnetic induction by the solar wind, Science, 172, 256-258, 1971c.

Sonett, C.P., B.F. Smith, D.S. Colburn, G. Schubert, and K. Schwartz, The induced magnetic field of the moon: conductivity profiles and inferred temperature, Proc. Third Lunar Sci. Conf., Vol. 3, The M.I.T. Press, in press, 1972a.

Sonett, C.P., B.F. Smith, D.S. Colburn, G. Schubert, and K. Schwartz, Lunar electrical conductivity-reply, Nature, in press, 1972b.

Spreiter, J.R., and A.Y. Alksne, Solar wind flow past objects in the solar system, in Annual Review of Fluid Mechanics, Vol. 2, pp. 313-354, 1970.

Stratton, J.A., Electromagnetic Theory, McGraw Hill, New York, 1941.

FIGURE CAPTIONS

Figure 1. Geometry of the theoretical model. The Moon has radius a with a spherical core of infinite electrical conductivity, $\sigma=\infty$, surrounded by a nonconducting shell of thickness (a-b). A cylindrical nonconducting cavity of radius a extends downstream from the Moon. The coordinates r, θ , φ are spherical, ρ, φ, z are cylindrical coordinates, with the origin of both coordinate systems at the center of the Moon and the z-axis coinciding with the cylinder axis. The external field is uniform and is either normal to the cavity axis, i.e. in the y-direction ($\varphi = \pi/2$) say, or parallel to the cavity axis. The variable core radius allows investigation of waves of different frequency which are excluded from different portions of the Moon.

Figure 2. The magnetic field component H_r and the SSV approximation to H_r as a function of position on the dark side lunar surface, r=a, $0<\theta< 90°$. The external field has unit amplitude and is parallel to the cylinder axis. The antisolar point is $\theta=0°$ while $\theta=90°$ is the limb. Note the increase in the radial field above the SSV value, the local minimum in the

Figure 2 (continued)

field near the antisolar point and the field maximum near the limb, the latter two phenomena for large b/a.

Figure 3. The magnetic field H_θ on the lunar surface as a function of θ for various b/a. The external field has unit amplitude and is aligned with the cavity axis. The field according to the SSV approximation is shown for b/a = 0.5 and 0.9. The field from the SSP approximation is virtually identical to the asymmetric field for $90° < \theta < 180°$. There is considerable amplification of H_θ on the lunar dark side. Further the amplification is asymmetric with respect to the terminator. Both the magnitude of the amplification and the extent of the asymmetry in the lunar response increase with b/a.

Figure 4. The radial magnetic field on the lunar dark side surface with b/a as a parameter when the external field of unit amplitude is aligned normal to the cavity axis. The radial field according to the SSV approximation is also shown. On the lunar front side, H_r is identical to that component of the external field. The radial field is viewed in the plane of the external field and the cylinder axis. The field

Figure 4 (continued)

is reduced below the SSV value near the antisolar point but exceeds the SSV value near the terminator. For b/a = 0.9 the field is essentially zero within 60° of the antisolar point.

Figure 5. The magnetic field component H_θ on the lunar surface vs. θ for various b/a in the case of unit external field normal to the cavity axis. The field according to the SSV approximation for b/a = 0.9 is shown for $0<\theta<90°$ and H_θ from the SSP approximation for b/a = 0.8 and 0.9 is shown for $90°<\theta<180°$. The field is viewed in the plane of the external field and the cavity axis. On the front side near the subsolar point H_θ is reduced below its SSP value, while on the dark side near the antisolar point H_θ is amplified above its SSV value. The field has a zero forward of the terminator as a result of the redistribution in the lunar interior of field lines from the sunward to the dark side hemisphere.

Figure 6. The field H_z on the cavity boundary $\rho=a$ as a function of distance downstream from the limb with b/a as a parameter. The unit external field is parallel to the cavity axis. Note the attenuation in H_z with

Figure 6 (continued)

distance from the limb; beyond about one lunar radius H_z is essentially zero. The figure also shows the distribution of azimuthal surface current density $K_\varphi = H_z$.

Figure 7. The field components H_z and H_φ , or alternatively the surface current densities $K_\varphi = H_z$ and $K_z = H_\varphi - 1$, on the cavity boundary $\rho=a$ as a function of z for various b/a. The unit external field is perpendicular to the cavity axis. The currents K_φ or fields H_z decay monotonically with distance downstream from the terminator. The currents K_z or fields H_φ attain a local maximum downstream from the limb before decaying to vanishingly small values.

Figure 8. The North-South tangential transfer function vs. solar longitude or local time with b/a as a parameter. The curves also represent H_φ for a unit external field perpendicular to the cavity axis if H_φ is viewed in the plane containing the cylinder axis and the normal to the external field. Values for the SSP and SSV approximations are also shown. For clarity of the figure, the b/a parameter has been omitted from the SSV lines. These values are b/a = 0.6, 0.7, 0.8 and 0.9, proceeding in order from the lowest to the highest

Figure 8 (continued)

SSV line. The transfer function or H_φ is independent of θ in the spherically symmetric approximations. Note the reduction in front side amplification below the SSP value and the increase in the dark side amplification above the SSV value.

Figure 9. The radial transfer function vs. solar longitude for several b/a. The external field is at 45° to the cavity axis and in the ecliptic plane and $\varphi = 90°$. For the entire front side, the radial transfer function is unity. On the lunar dark side, the transfer function shows a minimum about 30° from the antisolar point. The transfer function in the SSV approximation is independent of solar longitude.

Figure 10. The fields H_θ , H_φ or alternatively the tangential transfer function at the subsolar point $\theta = 180°$ and at the antisolar point $\theta=0°$ as a function of core size. The cavity amplification of fields at the antisolar point and the reduced amplification of fields at the subsolar point due to field line leakage into the cavity become increasingly important for larger cores, corresponding to waves whose effective exclusion depths are progressively shallower.

Figure 11. The radial transfer function at the antisolar point vs. b/a together with the SSV approximation. For a given lunar conductivity model the SSV approximation overestimates the induction.

Figure 12. The variation with b/a of the North-South transfer function at the limb. Both SSV and SSP approximations are also shown. The North-South magnetic field shows considerable amplification at the limb with values closer to those of the SSP than to those of the SSV approximation.

APPENDIX A

ANALYTIC SOLUTION FOR EXTERNAL MAGNETIC FIELD NORMAL TO THE CAVITY AXIS

The potential in the insulating shell Ω^I is

$$\Omega^I = \sum_{\ell=1}^{\infty} \left(A_\ell r^\ell + B_\ell r^{-\ell-1}\right) P_\ell^1 (\cos\theta) \sin\varphi \quad , \tag{A.1}$$

where A_ℓ and B_ℓ are coefficients to be determined as part of the solution, and $P_\ell^1(\cos\theta)$ are the associated Legendre functions of order 1 (the sign convention used here is such that for example $P_1^1(\cos\theta) = \sin\theta$). The φ dependence of Ω^1 follows from that of the external magnetic field which is

$$\underline{\hat{r}} \sin\theta \sin\varphi + \underline{\hat{\theta}} \cos\theta \sin\varphi + \underline{\hat{\varphi}} \cos\varphi \quad ,$$

or

$$\underline{\hat{\rho}} \sin\varphi + \underline{\hat{\varphi}} \cos\varphi \quad ,$$

where $\underline{\hat{r}}$, $\underline{\hat{\theta}}$, $\underline{\hat{\varphi}}$ and $\underline{\hat{\rho}}$, $\underline{\hat{\varphi}}$, $\underline{\hat{z}}$ are the unit vectors of the spherical and cylindrical coordinate systems, respectively. The magnetic field in the shell is

$$H_r^I = \sum_{\ell=1}^{\infty} \left\{\ell A_\ell r^{\ell-1} - (\ell+1) B_\ell r^{-\ell-2}\right\} P_\ell^1(\cos\theta)\sin\varphi \quad , \tag{A.2}$$

$$H_\theta^I = \sum_{\ell=1}^{\infty} \left(A_\ell r^{\ell-1} + B_\ell r^{-\ell-2}\right) \frac{dP_\ell^1(\cos\theta)}{d\theta} \sin\varphi \quad , \qquad (A.3)$$

$$H_\varphi^I = \sum_{\ell=1}^{\infty} \left(A_\ell r^{\ell-1} + B_\ell r^{-\ell-2}\right) \frac{P_\ell^1(\cos\theta)}{\sin\theta} \cos\varphi \quad . \qquad (A.4)$$

The coefficients A_ℓ and B_ℓ are related by the condition that the radial component of magnetic field be zero on $r = b$

$$\ell\, A_\ell b^{\ell-1} - (\ell+1)\, B_\ell b^{-\ell-2} = 0 \quad . \qquad (A.5)$$

The normal component of magnetic field must be $\sin\theta \sin\varphi$ on $r = a$, $\frac{\pi}{2} \le \theta \le \pi$. For the case of spherically symmetric plasma confinement(SSP), this condition is applied over the entire range of θ, i.e. 0 to π . The solution is then straightforward with

$$A_1 = \frac{a^3}{a^3-b^3} \; , \; B_1 = \frac{a^3b^3/2}{a^3-b^3} \; , \; A_\ell, \; B_\ell = 0 \text{ for } \ell \ge 2 \quad , \qquad (A.6)$$

and in the insulating shell, region I ,

$$H_r = \frac{a^3 \sin\theta \sin\varphi}{(a^3-b^3)} \left(1 - \frac{b^3}{r^3}\right) \quad , \qquad (A.7)$$

$$H_\theta = \frac{a^3 \cos\theta \sin\varphi}{(a^3-b^3)} \left(1 + \frac{b^3}{2r^3}\right) \quad , \qquad (A.8)$$

$$H_{\varphi} = \frac{a^3 \cos\varphi}{(a^3-b^3)} \left(1 + \frac{b^3}{2r^3}\right) \quad . \qquad (A.9)$$

In the spherically symmetric vacuum approximation (SSV) it is simple to verify that

$$A_1 = 1, \quad B_1 = \frac{b^3}{2}, \; A_\ell, \; B_\ell = 0 \quad \text{for} \quad \ell \geq 2 \quad , \qquad (A.10)$$

and in region I

$$H_r = \sin\theta \sin\varphi \left(1 - \frac{b^3}{r^3}\right) \quad , \qquad (A.11)$$

$$H_{\theta} = \cos\theta \sin\varphi \left(1 + \frac{b^3}{2r^3}\right) \quad , \qquad (A.12)$$

$$H_{\varphi} = \cos\varphi \left(1 + \frac{b^3}{2r^3}\right) \quad . \qquad (A.13)$$

The potential in region II, the cavity, is given by

$$\Omega^{II} = \rho \sin\varphi + \sin\varphi \sum_{n=1}^{\infty} C_n \, e^{-k_n z} \, J_1(k_n \rho) \quad , \qquad (A.14)$$

where C_n are coefficients to be determined in the solution, J_1 is the Bessel function of order 1 and $k_n a$ is the nth zero of $J_1'(k_n a) = 0$ (the prime denoting the derivative). The magnetic field is

$$H_{\rho}^{II} = \sin\varphi + \sin\varphi \sum_{n=1}^{\infty} C_n e^{-k_n z} \, k_n \, J_1'(k_n \rho) \quad , \qquad (A.15)$$

$$H_{\varphi}^{II} = \cos\varphi + \cos\varphi \sum_{n=1}^{\infty} C_n e^{-k_n z} \rho^{-1} J_1(k_n \rho) \quad , \qquad (A.16)$$

$$H_z^{II} = - \sin\varphi \sum_{n=1}^{\infty} C_n k_n e^{-k_n z} J_1(k_n \rho) \quad . \qquad (A.17)$$

This solution automatically satisfies the continuity of H_ρ on the cavity boundary $\rho = a$ since $J_1'(k_n a) = 0$. To apply the boundary conditions on the hemispherical surface $r = a$, $0 \le \theta \le \pi/2$, (A.14) - (A.17) are most conveniently rewritten in terms of spherical coordinates. With the aid of an identity due to Cooke [1956] we find

$$\Omega^{II} = r\sin\theta \sin\varphi + \sum_{\ell=1}^{\infty} C_\ell \sum_{n=1}^{\infty} \frac{(k_\ell r)^n (-1)^{n+1}}{(n+1)!} P_n^1(\cos\theta)\sin\varphi, \qquad (A.18)$$

$$H_r^{II} = \sin\theta \sin\varphi + \sum_{\ell=1}^{\infty} C_\ell \frac{\sin\varphi}{r} \sum_{n=1}^{\infty} \frac{(-1)^{n+1} n}{(n+1)!} (k_\ell r)^n P_n^1(\cos\theta), \qquad (A.19)$$

$$H_\theta^{II} = \cos\theta \sin\varphi + \sum_{\ell=1}^{\infty} C_\ell \frac{\sin\varphi}{r} \sum_{n=1}^{\infty} \frac{(-1)^{n+1}}{(n+1)!} (k_\ell r)^n \frac{dP_n^1(\cos\theta)}{d\theta} \quad , \qquad (A.20)$$

$$H_\varphi^{II} = \cos\varphi + \sum_{\ell=1}^{\infty} C_\ell \frac{\cos\varphi}{r} \sum_{n=1}^{\infty} \frac{(-1)^{n+1}}{(n+1)!} (k_\ell r)^n \frac{P_n^1(\cos\theta)}{\sin\theta} \quad , \qquad (A.21)$$

Continuity of H_r on r = a yields

$$\sum_{\ell=1}^{\infty} \left\{ \ell A_\ell \, a^{\ell-1} - (\ell+1) B_\ell a^{-\ell-2} \right\} P_\ell^1(\cos\theta) - \sin\theta =$$

$$\sum_{\ell=1}^{\infty} \frac{C_\ell}{a} \sum_{n=1}^{\infty} \frac{(-1)^{n+1} n}{(n+1)!} (k_\ell a)^n P_n^1(\cos\theta) \quad , \quad 0 < \theta \, \pi/2$$

or 0 $\quad , \frac{\pi}{2} < \theta < \pi$ (A.22)

Equation (A.22) leads to the following relationship among the unknown coefficients

$$\frac{2\ell'(\ell'+1)}{(2\ell'+1)} \left\{ \ell' A_{\ell'} a^{\ell'-1} - (\ell'+1) B_{\ell'} a^{-\ell'-2} \right\} - \frac{4}{3} \delta_{\ell',1}$$

(A.23)

$$= \sum_{\ell=1}^{\infty} \frac{C_\ell}{a} \sum_{n=1}^{\infty} \frac{(-1)^{n+1} n}{(n+1)!} (k_\ell a)^n P_{n\ell'} \quad , \quad \ell' = 1, 2, 3 \cdots$$

where $\delta_{\ell',1} = 1$ if $\ell' = 1$

$= 0$ if $\ell' \neq 1$, (A.24)

$$P_{\ell\ell'} = \frac{P_{\ell'}^1(0) \frac{dP_\ell^1}{d\cos\theta}(0) - P_\ell^1(0) \frac{dP_{\ell'}^1}{d\cos\theta}(0)}{\ell(\ell+1) - \ell'(\ell'+1)} \quad , \ell \neq \ell'$$

$$= \frac{\ell'(\ell'+1)}{(2\ell'+1)} \quad , \ell = \ell' \, , \qquad \text{(A.25)}$$

In (A.25) the argument of the associated Legendre functions and their derivatives is $\cos\theta = 0$.

On r=a, $0<\theta< \pi/2$, H_θ and H_φ are continuous. It is sufficient to apply one of these conditions, the other being redundant. Continuity of H_φ leads to

$$\sum_{\ell=1}^{\infty} \left(A_\ell a^{\ell-1} + B_\ell a^{-\ell-2}\right) P_\ell^1(\cos\theta) = \sin\theta + \sum_{\ell=1}^{\infty} \frac{C_\ell}{a} \sum_{n=1}^{\infty} \frac{(-1)^{n+1}}{(n+1)\,!} (k_\ell a)^n P_n^1(\cos\theta) \quad , \qquad (A.26)$$

for $0<\theta< \pi/2$. To generate a set of equations for the unknown coefficients from (A.26) it must be noted that on the range of θ given the odd associated Legendre functions form a complete set. Expanding (A.26) in terms of this set of odd associated Legnedre functions we find

$$\sum_{\ell=1}^{\infty} \left(A_\ell a^{\ell-1} + B_\ell a^{-\ell-2}\right) P_{\ell\ell'} = \frac{2}{3}\,\delta_{\ell',1} + \sum_{\ell=1}^{\infty} \frac{C_\ell}{a} \sum_{n=1}^{\infty} \frac{(-1)^{n+1}}{(n+1)!} (k_\ell a)^n P_{n\ell'} \quad , \qquad (A.27)$$

for $\ell' = 1,3,5,\cdots$

Equations (A.5), (A.23) and (A.27) suffice to determine A_ℓ, B_ℓ and C_ℓ . After considerable algebraic manipulation, a single set of equations for C_ℓ may be derived

$$\sum_{m=1}^{\infty} \left(\frac{C_m}{a}\right) \left\{ \frac{(k_m a)^{\ell'}\ \ell'(\ell'+1)}{(2\ell'+1)(\ell'+1)!} \frac{\left(\frac{\alpha_{\ell'}}{2}\ \ell' - 1\right)}{P_{\ell'}^1(0)} \right.$$

$$+ \sum_{n\ \text{even}} \frac{(k_m a)^n}{(n+1)!} \frac{\frac{dP_n^1}{d\cos\theta}(0)\ \left(\frac{n}{2}(\alpha_{\ell'} + \alpha_n) - 1\right)}{\ell'(\ell'+1) - n(n+1)}$$

$$+ \sum_{n\ \text{odd}} \frac{(k_m a)^n n\ P_n^1(0)}{(n+1)!} \sum_{\ell\ \text{even}} \frac{\alpha_\ell (2\ell+1)}{2\ell(\ell+1)} \cdot$$

$$\left. \frac{\left(\frac{dP_\ell^1}{d\cos\theta}(0)\right)^2}{\left[\ell(\ell+1) - \ell'(\ell'+1)\right]\left[\ell(\ell+1) - n(n+1)\right]} \right\}$$

$$= \frac{2}{3}(1-\alpha_1)\ \delta_{\ell',1} \quad , \qquad \ell' = 1,3,5,\cdots \quad , \tag{A.28}$$

where

$$\alpha_\ell = \frac{1 + \frac{\ell}{\ell+1}\left(\frac{b}{a}\right)^{2\ell+1}}{\ell\left(1 - \left(\frac{b}{a}\right)^{2\ell+1}\right)} \quad . \tag{A.29}$$

Once C_ℓ is determined from (A.28), A_ℓ may be found from

$$A_\ell a^{\ell-1} = \frac{\sum_{m=1}^{\infty} \frac{C_m}{a} (k_m a)^\ell}{2\left(1-\left(\frac{b}{a}\right)^{2\ell+1}\right)(\ell+1)!} + \frac{\delta_{\ell,1}}{1-\left(\frac{b}{a}\right)^3}$$

$$+ \frac{(2\ell+1)P_\ell^1(0)}{2\ell^2(\ell+1)\left(1-\left(\frac{b}{a}\right)^{2\ell+1}\right)} \sum_{m=1}^{\infty} \frac{C_m}{a} \sum_{n\,\text{even}}$$

$$\frac{n(k_m a)^n \frac{dP_n^1}{d\cos\theta}(0)}{(n+1)!\left\{\ell(\ell+1)-n(n+1)\right\}} \quad , \qquad (A.30)$$

for ℓ odd and

$$A_\ell a^{\ell-1} = \frac{\sum_{m=1}^{\infty} \frac{C_m}{a} (k_m a)^\ell}{2\left(1-\left(\frac{b}{a}\right)^{2\ell+1}\right)(\ell+1)!}$$

$$+ \frac{(2\ell+1)\frac{dP_\ell^1}{d\cos\theta}(0)}{2\ell^2(\ell+1)\left(1-\left(\frac{b}{a}\right)^{2\ell+1}\right)} \sum_{m=1}^{\infty} \frac{C_m}{a} \sum_{n\,\text{odd}}$$

$$\frac{n(k_m a)^n P_n^1(0)}{(n+1)!\left\{\ell(\ell+1)-n(n+1)\right\}} \quad , \qquad (A.31)$$

for ℓ even. With C_ℓ and A_ℓ determined, B_ℓ follows from (7). The zeros of J_1' are tabulated in Abromowitz and Stegun [1964].

The infinite set of algebraic equations has been truncated and solved numerically. Convergence of the solution has been assured by increasing the size of the set until a further increase in size produced a negligible change in the results.

APPENDIX B

ANALYTIC SOLUTION FOR EXTERNAL MAGNETIC FIELD PARALLEL TO CAVITY AXIS

The external magnetic field is

$$\hat{z} = \cos\theta\ \hat{r} - \sin\theta\ \hat{\theta} \quad .$$

Thus the magnetic potential in the lunar shell is

$$\Omega^I = \sum_{\ell=1}^{\infty} \left(A_\ell r^\ell + B_\ell r^{-\ell-1}\right) P_\ell(\cos\theta) \quad , \qquad (A.32)$$

where $P_\ell(\cos\theta)$ are the Legendre polynomials and the magnetic field is given by

$$H_r^I = \sum_{\ell=1}^{\infty} \left(\ell A_\ell r^{\ell-1} - (\ell+1) B_\ell r^{-\ell-2}\right) P_\ell(\cos\theta) \quad , \qquad (A.33)$$

$$H_\theta^I = \sum_{\ell=1}^{\infty} \left(A_\ell r^{\ell-1} + B_\ell r^{-\ell-2}\right) \frac{dP_\ell(\cos\theta)}{d\theta} \quad . \qquad (A.34)$$

With the azimuthal symmetry characteristic of this external field alignment, all quantities are independent of φ and there is no azimuthal magnetic field. The coefficients A_ℓ and B_ℓ

must satisfy the condition (A.5)

The magnetic potential in the cavity is

$$\Omega^{II} = z + \sum_{n=1}^{\infty} C_n e^{-k_n' z} J_0(k_n' \rho) \quad , \qquad (A.35)$$

where J_0 is the Bessel function of order zero and $k_n' a$ is the nth zero of $J_0'(k_n' a) = 0$. From the gradient of (A.35) we find the magnetic field

$$H_\rho^{II} = \sum_{n=1}^{\infty} C_n e^{-k_n' z} k_n' J_0'(k_n' \rho) \quad , \qquad (A.36)$$

$$H_z^{II} = 1 - \sum_{n=1}^{\infty} k_n' C_n e^{-k_n' z} J_0(k_n' \rho) \quad . \qquad (A.37)$$

Note that H_ρ on the cavity boundary is identically zero. The magnetic field in the cavity can be written in terms of spherical coordinates using an identity from Cooke [1956] similar to the one employed in Appendix A

$$H_r^{II} = \sum_{\ell=1}^{\infty} \frac{C_\ell}{r} \sum_{n=1}^{\infty} \frac{(-1)^n (k_\ell' r)^n}{(n-1)!} P_n(\cos\theta) + \cos\theta \quad , \qquad (A.38)$$

$$H_\theta^{II} = \sum_{\ell=1}^{\infty} \frac{C_\ell}{r} \sum_{n=1}^{\infty} (-1)^n \frac{(k_\ell' r)^n}{n!} \frac{dP_n}{d\theta} (\cos\theta) - \sin\theta \quad . \qquad (A.39)$$

Equations (A.38) and (A.39) facilitate the application of the continuity conditions on the lunar dark side.

Continuity of H_r on $r = a$ yields

$$\sum_{\ell=1}^{\infty} \left\{\ell A_\ell a^{\ell-1} - (\ell+1)B_\ell a^{-\ell-2}\right\} P_\ell(\cos\theta) - \cos\theta =$$

$$\sum_{\ell=1}^{\infty} \frac{C_\ell}{a} \sum_{n=1}^{\infty} (-1)^n \frac{(k'_\ell a)^n}{(n-1)!} P_n(\cos\theta) \quad , \quad 0<\theta< \pi/2 \quad ,$$

$$\text{or} \quad 0 \quad , \quad \frac{\pi}{2} <\theta<\pi \quad . \qquad \text{(A.40)}$$

From (A.40) we find

$$\frac{2}{(2\ell'+1)} \left\{\ell' A_{\ell'} a^{\ell'-1} - (\ell'+1)B_{\ell'} a^{-\ell'-2}\right\} - \frac{2}{3}\delta_{\ell',1} =$$

$$\sum_{\ell=1}^{\infty} \frac{C_\ell}{a} \sum_{n=1}^{\infty} \frac{(-1)^n (k'_\ell a)^n}{(n-1)!} Q_{n\ell'} \qquad \ell'=1,2,3\cdots \qquad \text{(A.41)}$$

where

$$Q_{n\ell'} = \frac{1}{(2\ell'+1)} \qquad \text{if} \qquad \ell'=n$$

$$= \frac{P_{\ell'} \frac{dP_n}{d\cos\theta}(0) - P_n \frac{dP_{\ell'}}{d\cos\theta}(0)}{n(n+1)-\ell'(\ell'+1)} \quad . \qquad \text{(A.42)}$$

Continuity of H_θ on $r = a$ for $0<\theta< \pi/2$ yields

$$\sum_{\ell=1}^{\infty} \left(A_\ell a^{\ell-1}+B_\ell a^{-\ell-2}\right)P_\ell^1(\cos\theta)=\sin\theta+ \sum_{\ell=1}^{\infty} \frac{C_\ell}{a} \sum_{n=1}^{\infty} \frac{(-1)^n}{n!} (k_\ell' a)^n P_n^1(\cos\theta) \quad , \qquad (A.43)$$

which upon expansion in terms of the set of odd associated Legendre functions can be written

$$\sum_{\ell=1}^{\infty} \left(A_\ell a^{\ell-1}+B_\ell a^{-\ell-2}\right)P_{\ell\ell'}= \frac{2}{3} \delta_{\ell',1}+ \sum_{\ell=1}^{\infty} \frac{C_\ell}{a} \sum_{n=1}^{\infty} \frac{(-1)^n}{n!} (k_\ell' a)^n P_{n\ell'} \quad ,$$

$$\ell'=1,3,5,\cdots \quad . \qquad (A.44)$$

Equations (A.5), (A.41) and (A.44) determine A_ℓ, B_ℓ and C_ℓ for the aligned field case. In view of the detail presented in Appendix A, further algebraic reduction of the aligned field case will not be presented.

The SSP solution is

$$A_1 = \frac{a^3}{a^3-b^3} \quad , \quad B_1 = \frac{a^3b^3}{2(a^3-b^3)} \quad , \quad A_\ell, B_\ell=0 \quad \text{for } \ell\geq 2, \qquad (A.45)$$

$$H_r^I = \frac{a^3\cos\theta}{(a^3-b^3)} \left(1 - \frac{b^3}{r^3}\right) \quad , \qquad (A.46)$$

$$H_\theta^I = \frac{-a^3 \sin\theta}{(a^3-b^3)} \left(1 + \frac{b^3}{2r^3}\right) \quad . \qquad (A.47)$$

The SSV solution is

$$A_1=1 \ , \ B_1= b^3/2 \ , \ A_\ell=B_\ell=0 \quad \text{for} \quad \ell\geq 2 \quad , \qquad (A.48)$$

$$H_r^I = \cos\theta \left(1 - \frac{b^3}{r^3}\right) \quad , \qquad (A.49)$$

$$H_\theta^I = - \sin\theta\left(1 + \frac{b^3}{2r^3}\right) \quad . \qquad (A.50)$$

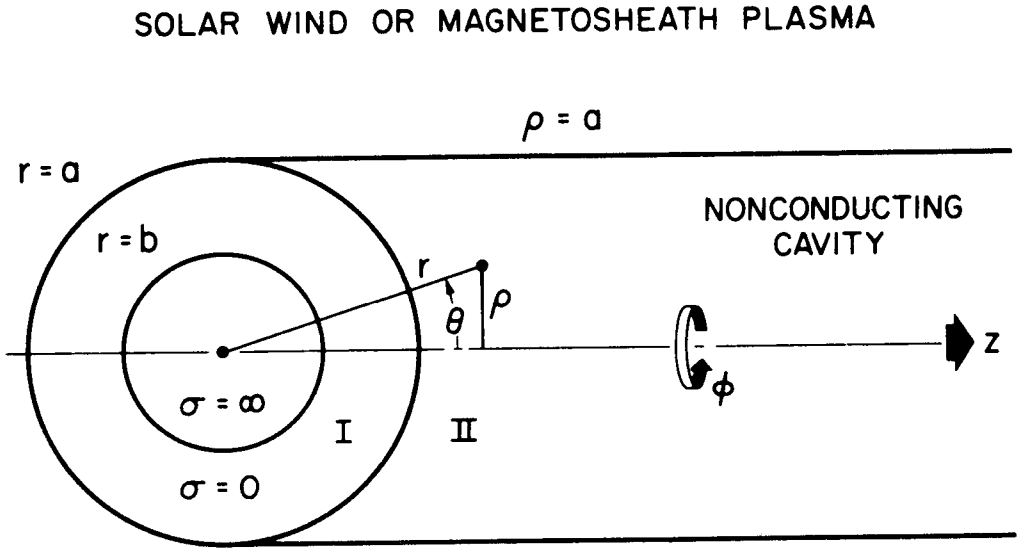
SOLAR WIND OR MAGNETOSHEATH PLASMA
ρ = a
r = a
r = b
NONCONDUCTING
CAVITY
r
θ
ρ
z
φ
σ = ∞
σ = 0
I
II

Fig.
1

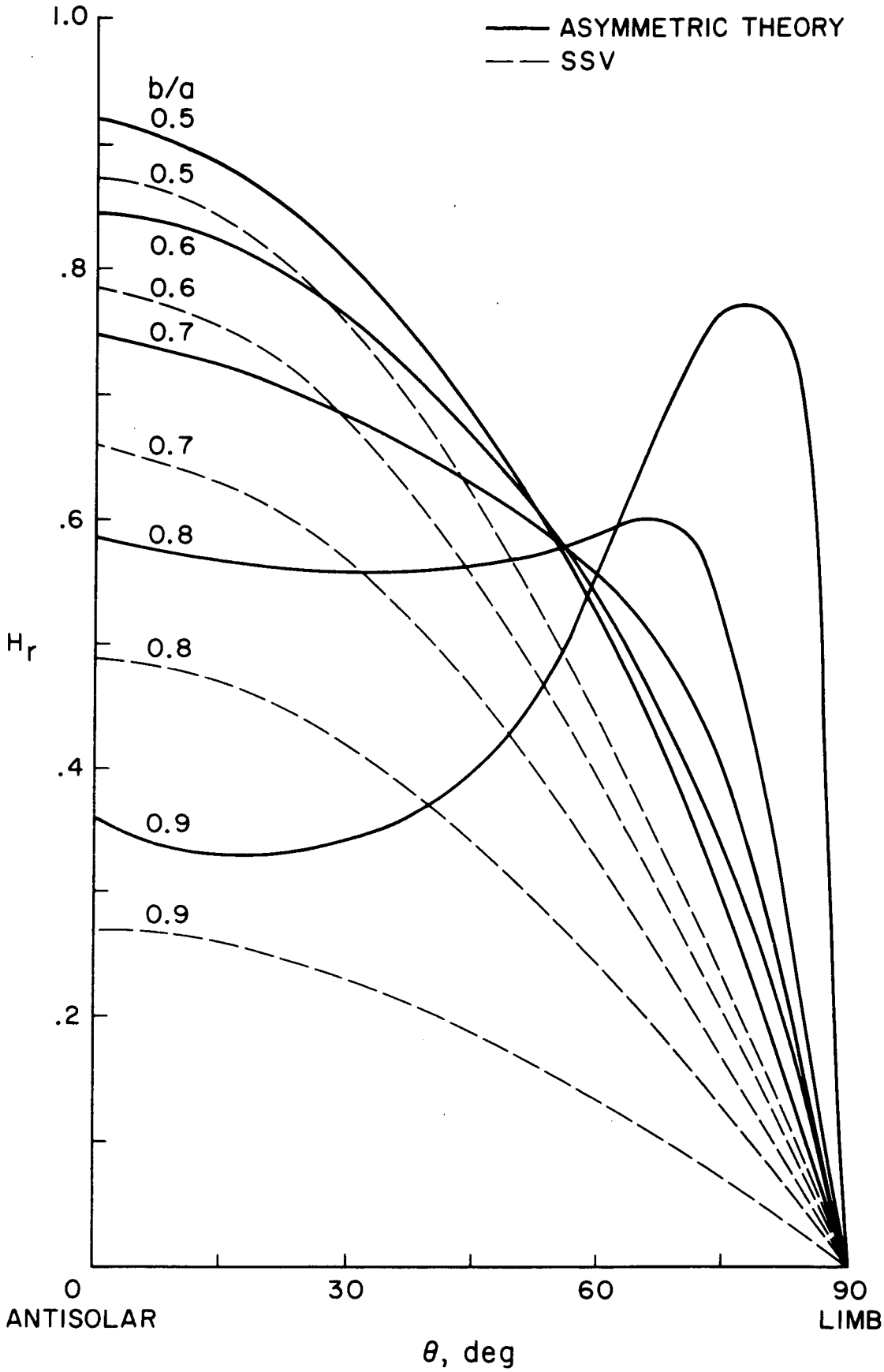
ASYMMETRIC THEORY
SSV
b/a
0.5
0.5
0.6
0.6
0.7
0.7
0.8
0.8
0.9
0.9
1.0
.8
.6
.4
.2
H_r
0
ANTISOLAR
30
60
90
LIMB
θ, deg

Fig. 2

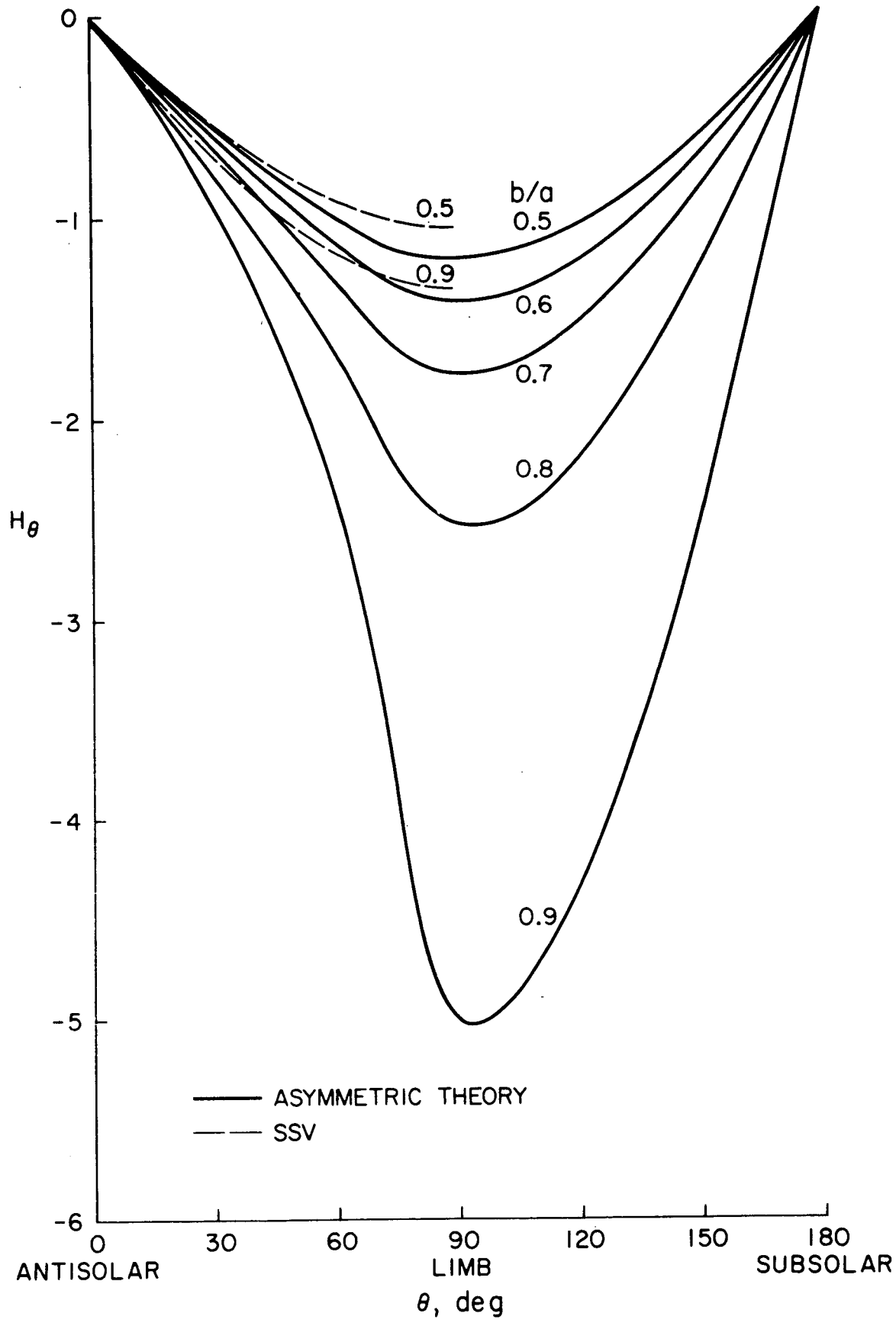
0
-1
-2
-3
-4
-5
-6
H_θ
b/a
0.5
0.5
0.9
0.6
0.7
0.8
0.9
ASYMMETRIC THEORY
SSV
0
30
60
90
120
150
180
ANTISOLAR
LIMB
SUBSOLAR
θ, deg

Fig. 3

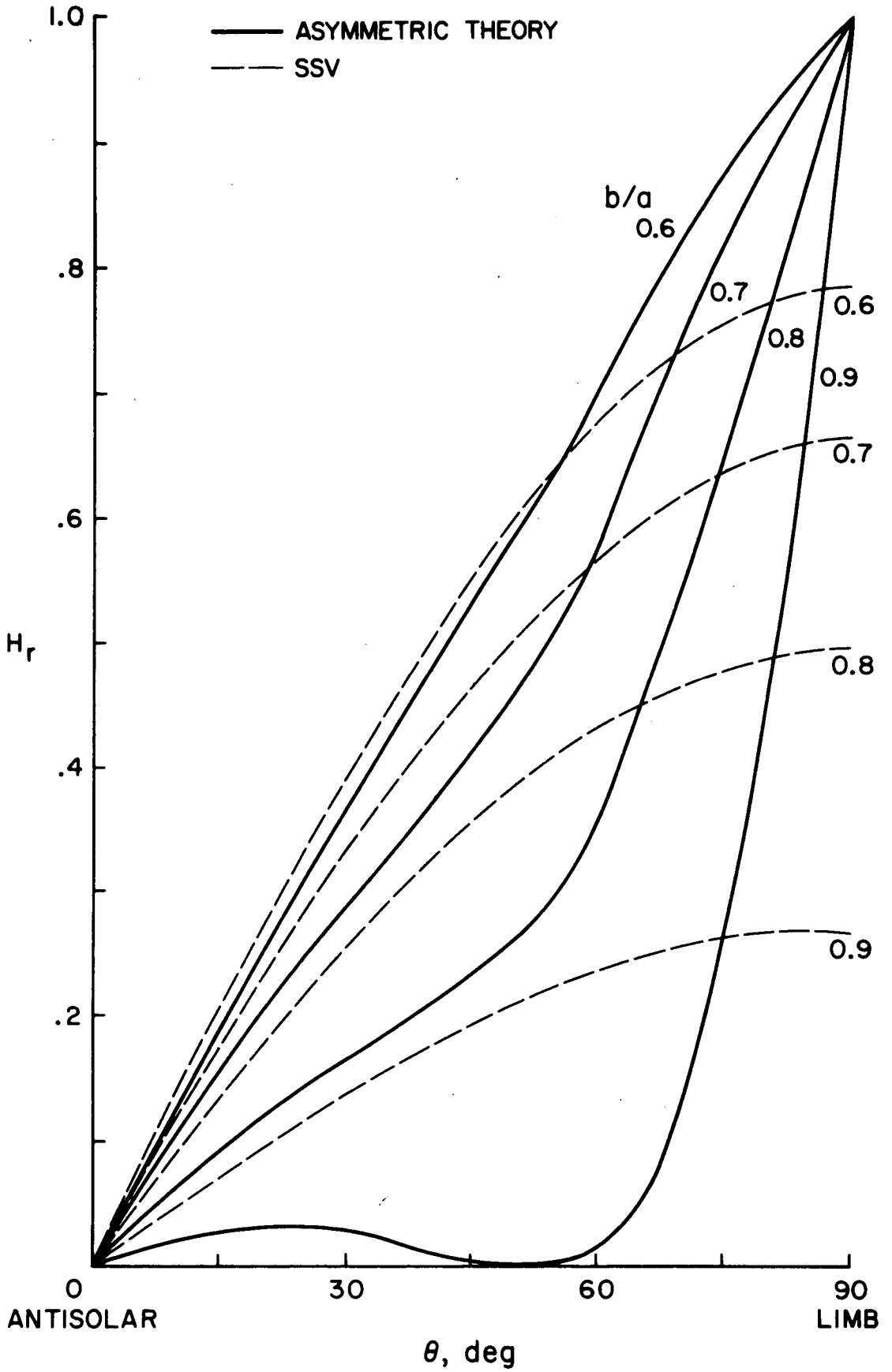
ASYMMETRIC THEORY
SSV
b/a
0.6
0.7
0.8
0.9
0.6
0.7
0.8
0.9
1.0
.8
.6
.4
.2
H_r
0
ANTISOLAR
30
60
90
LIMB
θ, deg

Fig. 4

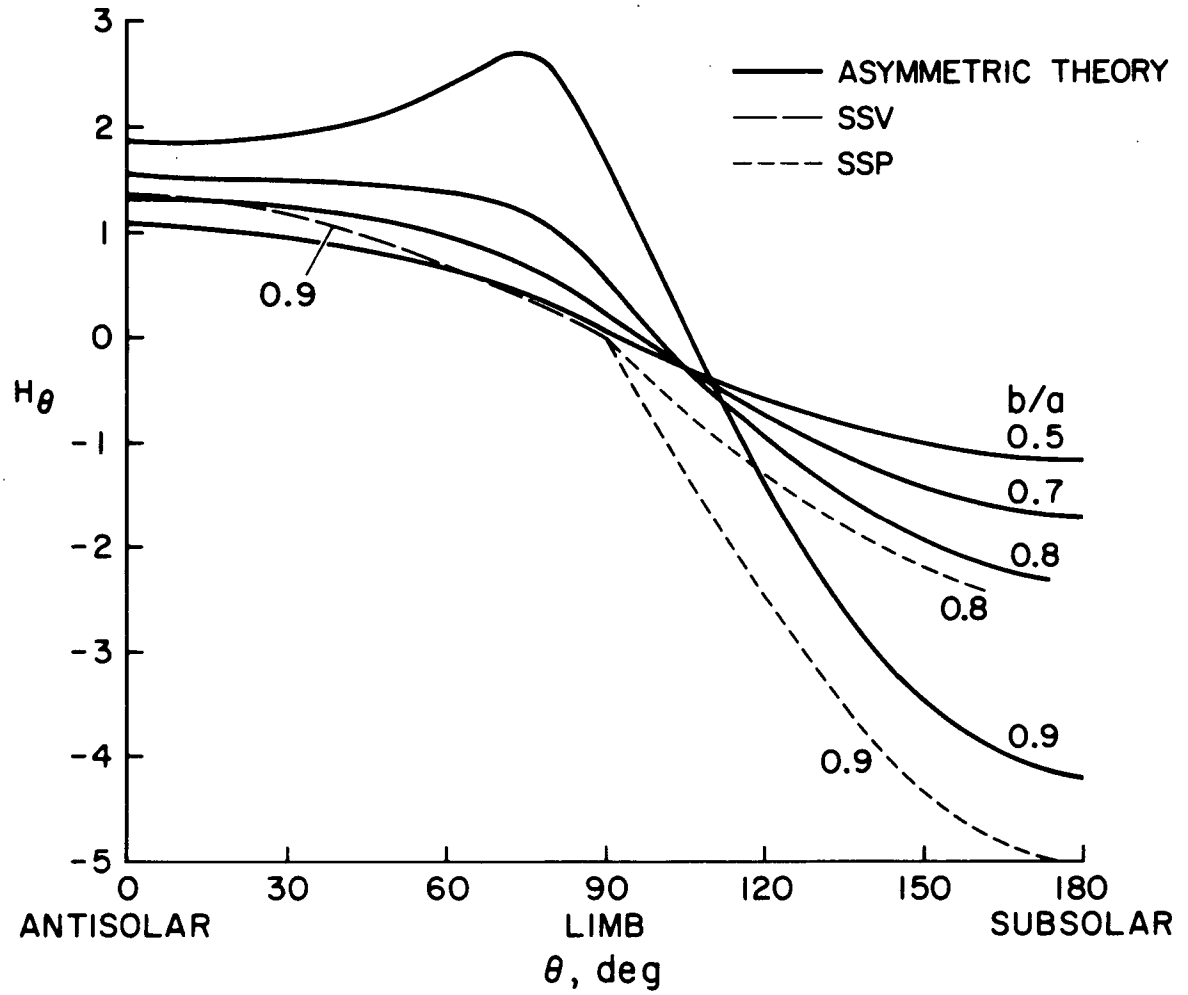
ASYMMETRIC THEORY
SSV
SSP
b/a
0.5
0.7
0.8
0.9
0.9
0.8
0.9
H_θ
3
2
1
0
-1
-2
-3
-4
-5
0
30
60
90
120
150
180
ANTISOLAR
LIMB
SUBSOLAR
θ, deg

Fig. 5

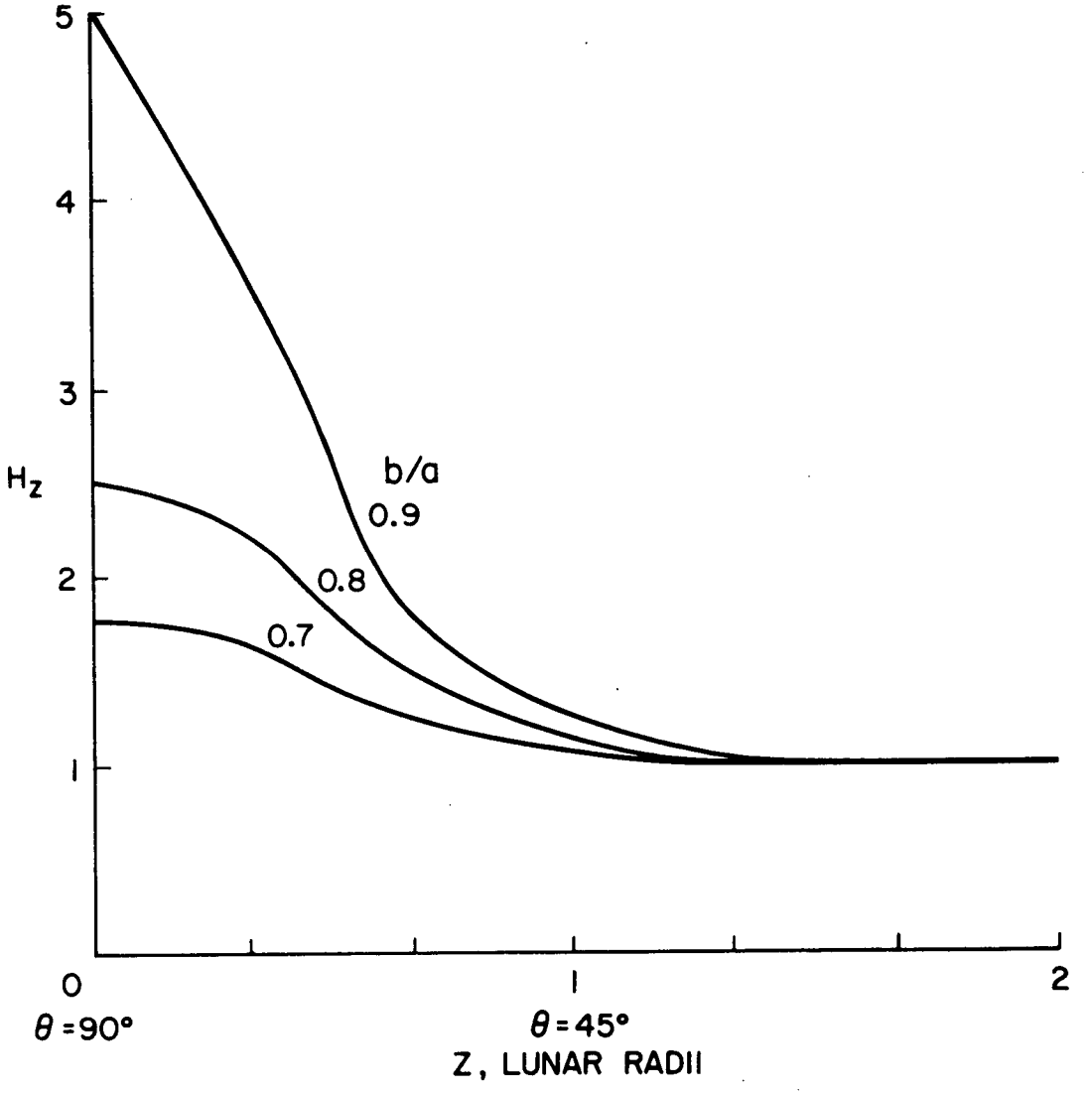

Fig. 6

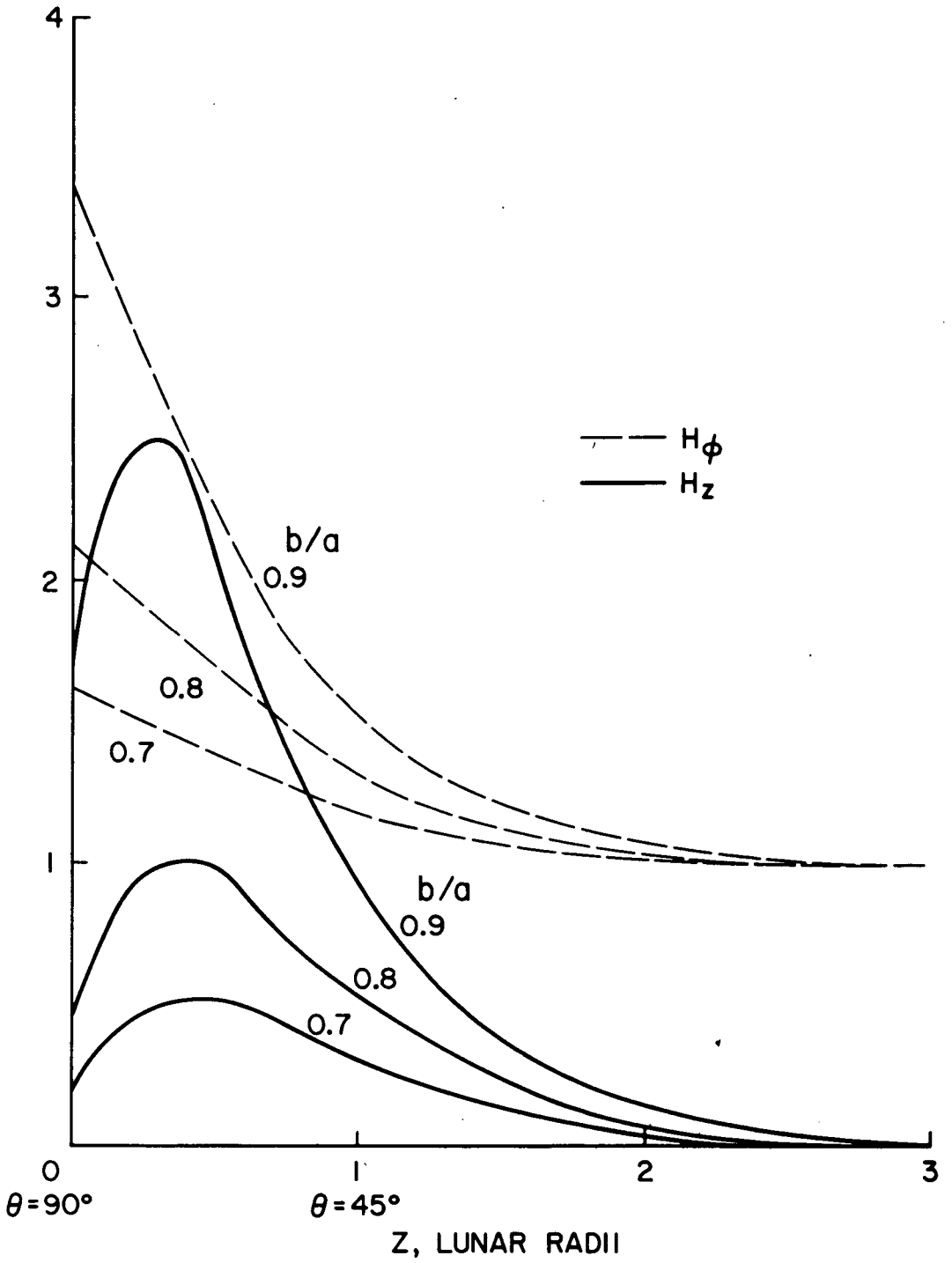

Fig. 7

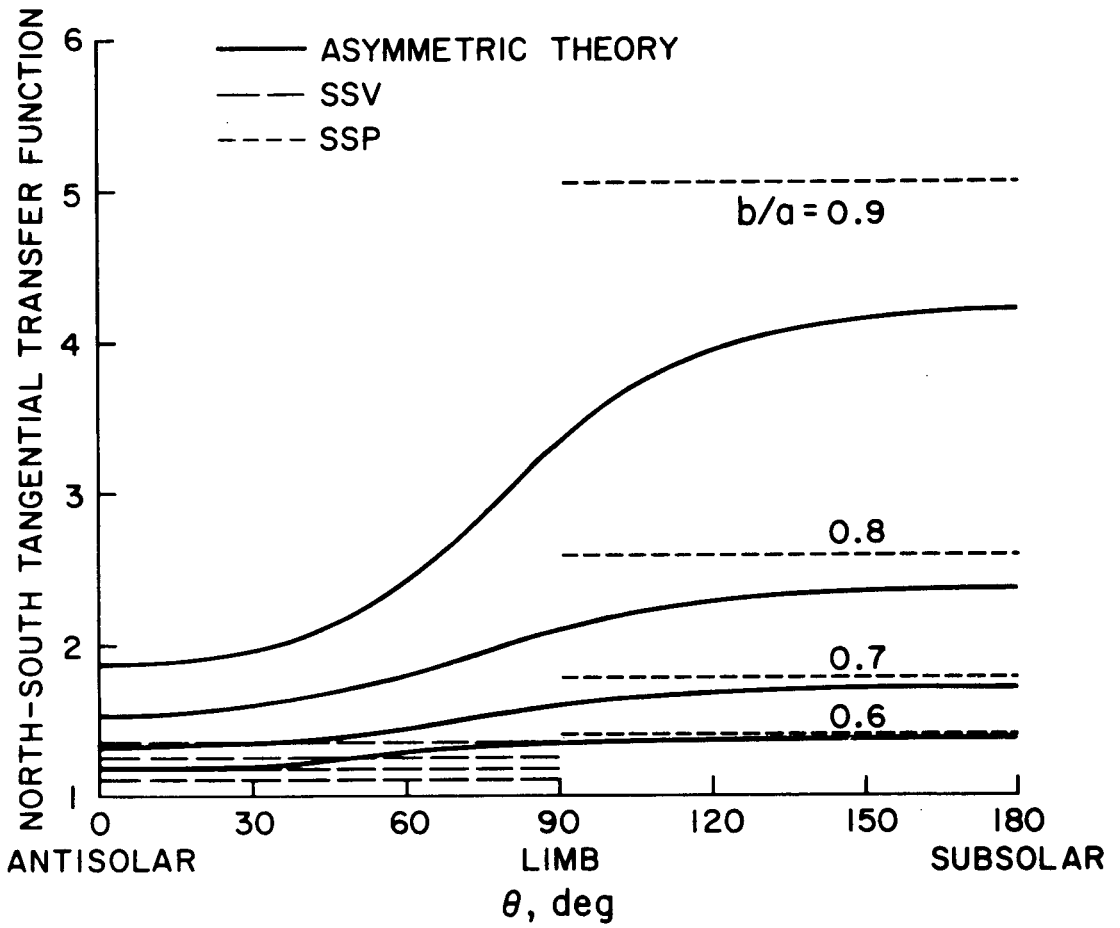
ASYMMETRIC THEORY
SSV
SSP
b/a = 0.9
0.8
0.7
0.6
NORTH-SOUTH TANGENTIAL TRANSFER FUNCTION
1
2
3
4
5
6
0
30
60
90
120
150
180
ANTISOLAR
LIMB
SUBSOLAR
θ, deg

Fig. 8

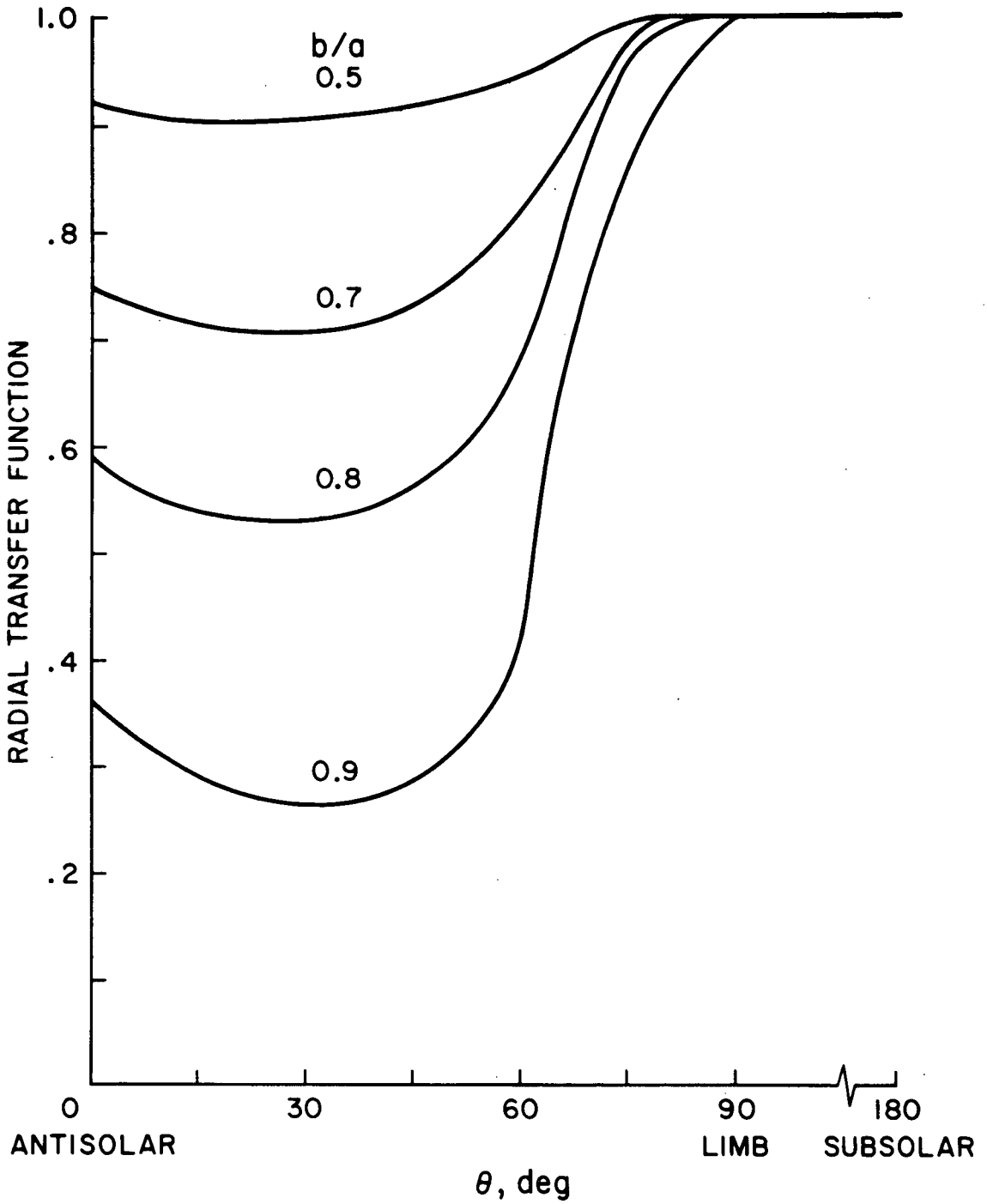
1.0
.8
.6
.4
.2
0
b/a
0.5
0.7
0.8
0.9
RADIAL TRANSFER FUNCTION
30
60
90
180
ANTISOLAR
LIMB
SUBSOLAR
θ, deg

Fig. 9

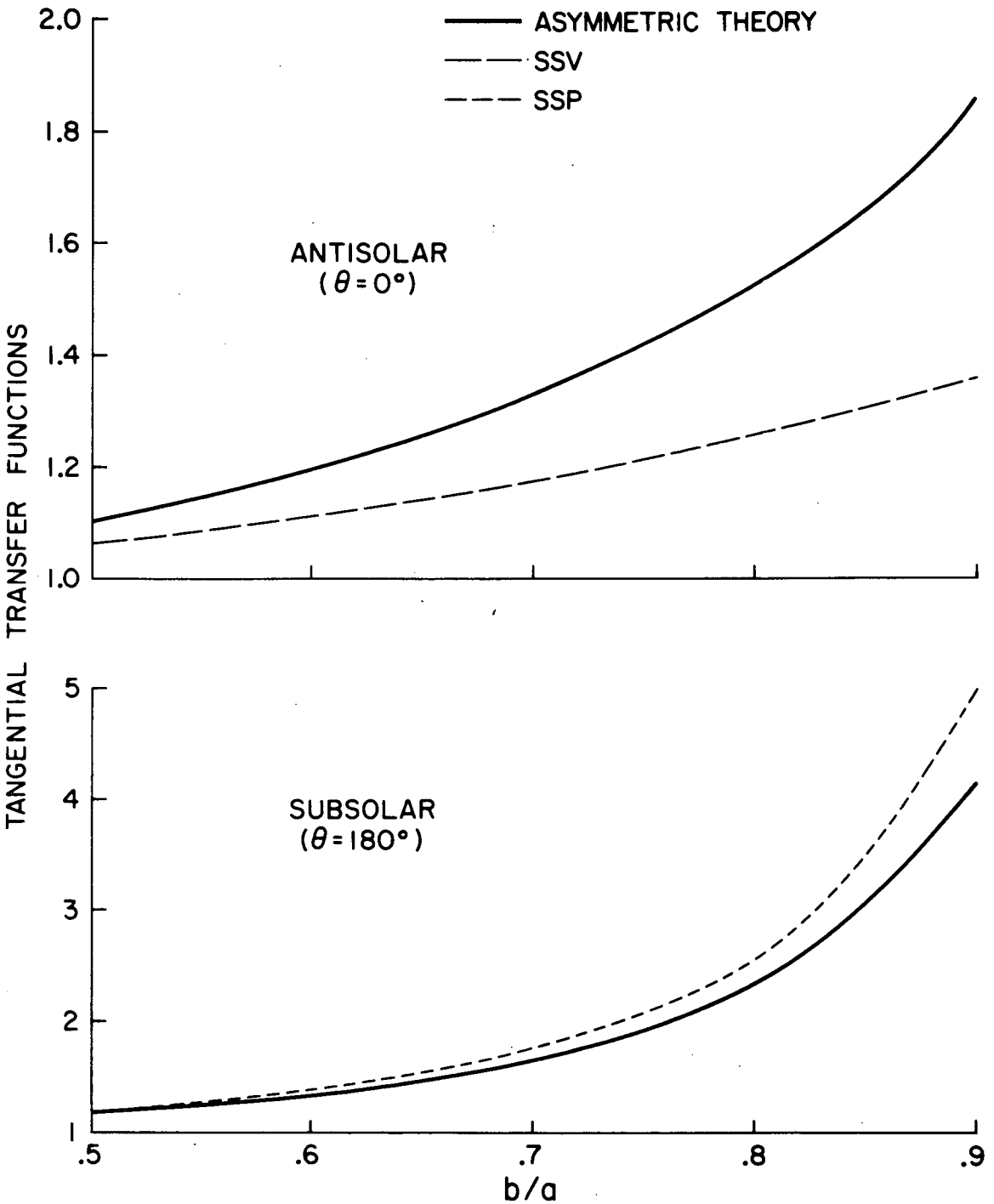
ASYMMETRIC THEORY
SSV
SSP
ANTISOLAR
(θ = 0°)
SUBSOLAR
(θ = 180°)
TANGENTIAL TRANSFER FUNCTIONS
2.0
1.8
1.6
1.4
1.2
1.0
5
4
3
2
1
.5
.6
.7
.8
.9
b/a

Fig. 10

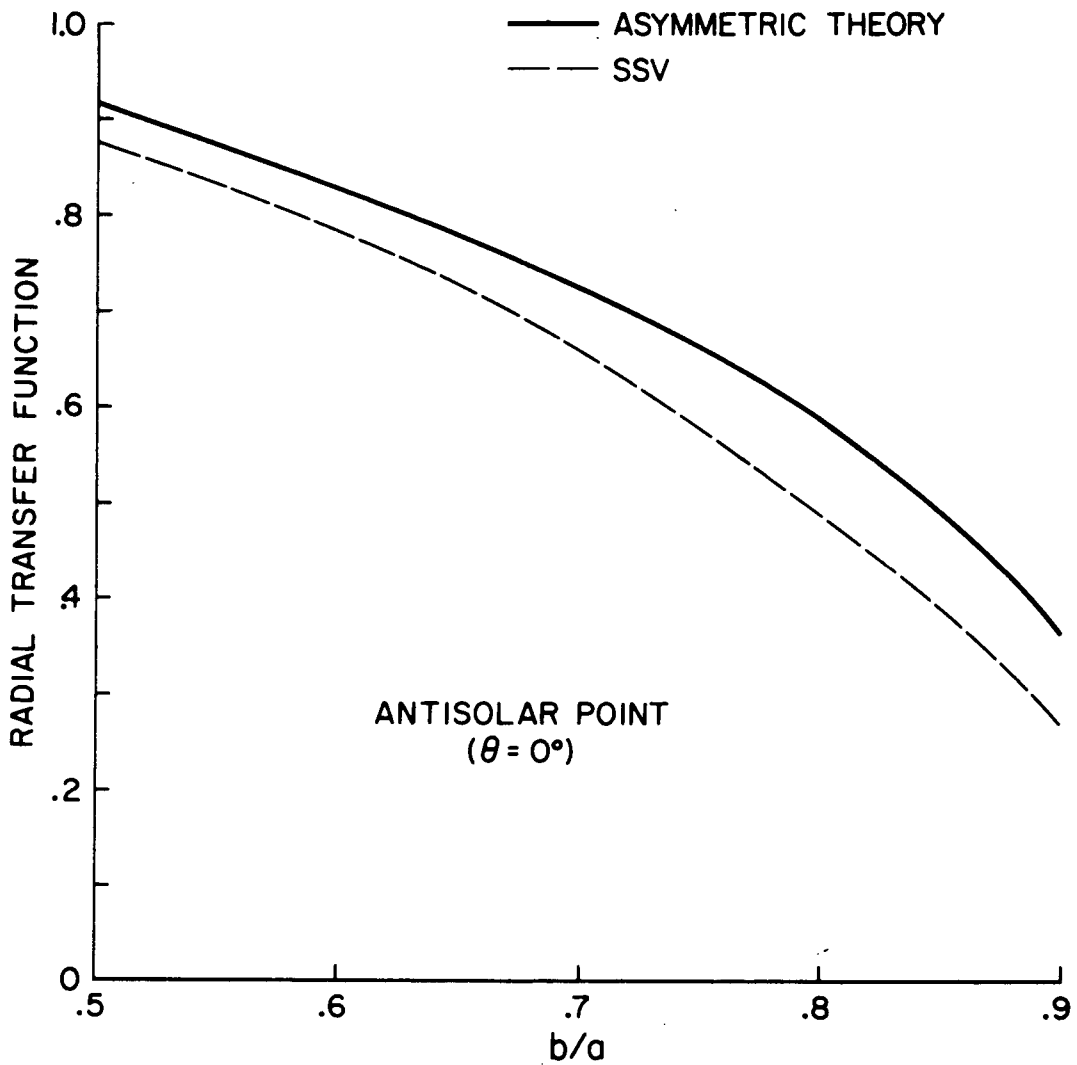
ASYMMETRIC THEORY
SSV
1.0
.8
.6
.4
.2
0
RADIAL TRANSFER FUNCTION
ANTISOLAR POINT
(θ = 0°)
.5
.6
.7
.8
.9
b/a

Fig. 11

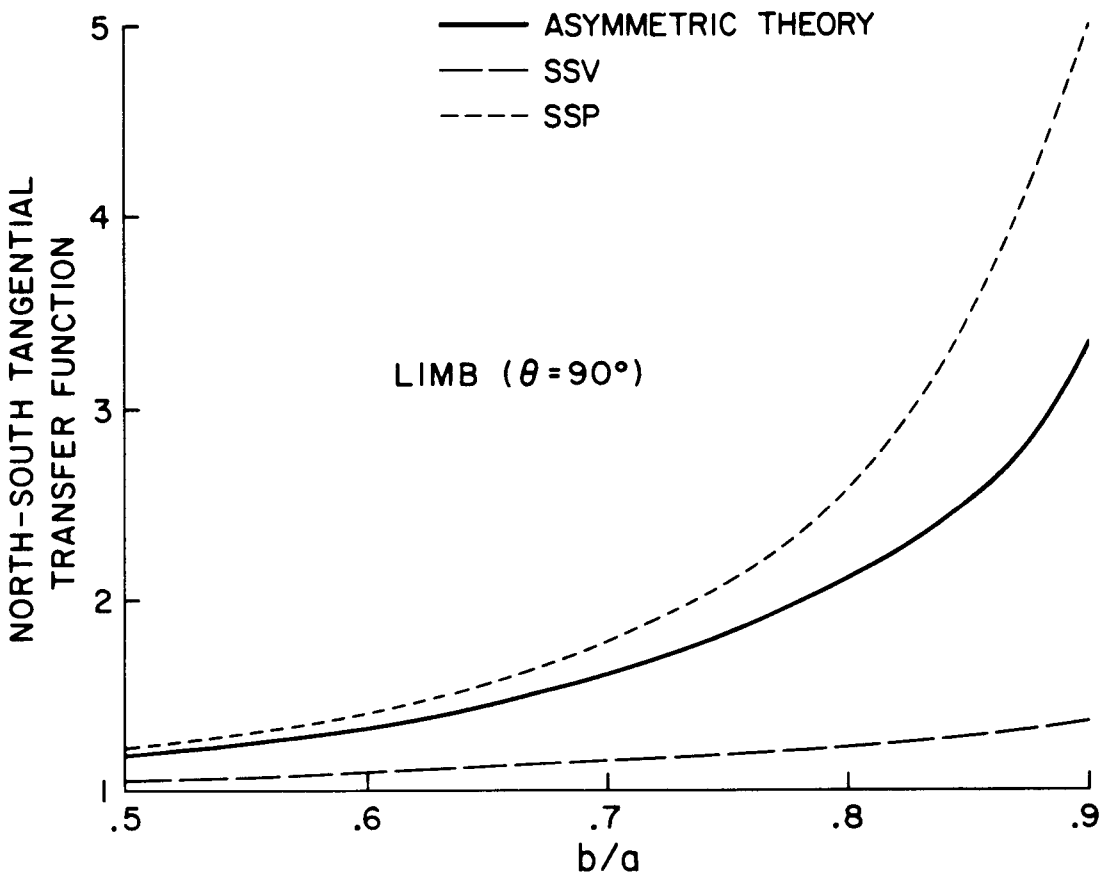

Fig. 12

NASA--ARC- Coml., Calif.